JOURNAL OF SPACECRAFT AND ROCKETS
Vol. 36, No. 4, July–August 1999

Forces for Rolling and Asymmetric Pinching of Pressurized Cylindrical Tubes

J. P. Fay* and C. R. Steele†
Stanford University, Stanford, California 94305-4035

The space application of inflatable structures makes desirable a better understanding of how membranes inflate from tightly packed arrangements. Two experiments determined the static forces and moments induced by internal pressure in a partially deployed membrane. The first experiment examined the forces at a fold or crease line. The second characterized the torque on a rolled-up membrane. In both experiments regions of nearly constant curvature dominated the deformed tube, which is consistent with general considerations of thin-shell behavior. This observation permits a simple approximation for the calculation of the volume of the deformed configuration. The volume can then be used in a potential energy formulation. The results from this formulation agree with the experimental measurements. Therefore, this formulation shows promise for simulating the inflation process with minimal computational effort.

Nomenclature

A = cross-sectional area of membrane
a = semimajor axis of elliptical section of membrane
E = Young's modulus of Mylar (measured value), 855 MPa
F = downward force on the blade
h = gap height between blade and base board
h_b = vertical distance from the bottom edge of the polyvinyl chloride (PVC) pipe to the roll, 14 mm
h_1 = contact height on left side of blade
h_2 = contact height on right side of blade
L = horizontal distance between the end of the PVC pipe and the center of the axle or blade
L_1 = axial distance between the centers of curvature of the top and bottom cross cylinders
L_2 = axial distance from the center of the top cross cylinder to the axle
L_3 = excess length to right side of blade or axle of deflated membrane
N_1 = axial stress resultant
N_2 = circumferential stress resultant
P = internal pressure
R = radius of inflated cylindrical Mylar tube, 30 mm
R_b = radius of curvature in the bottom cross-cylinder portion
R_t = radius of curvature in the top cross-cylinder portion of membrane
R_0 = radius of axle, 5 mm
s_0 = deflated tube length, 422 mm
T = torque about axle
t = membrane thickness, 32 μm
Vol = volume contained within the membrane
w = length of material that has slipped past the blade
x_{max} = limit of area integration
α = angle of rotation of the axle
Δx = axial shift of a point on the top of the membrane with respect to a point on the bottom of the membrane
Δz = flattening of membrane cross section
ε_1 = average strain in the long axis direction
ε_2 = average strain in the circumferential direction
θ_b = angle subtended by the bottom cross-cylinder portion
θ_t = angle subtended by the top cross-cylinder portion
μ = coefficient of friction between wood and Mylar
μ_{eff} = effective coefficient of friction for Mylar wrapped around a wood blade
ν = assumed Poisson's ratio, 0.3
Π = total potential energy
ρ = axial prestress parameter

Received 27 June 1997; revision received 18 July 1998; accepted for publication 23 December 1998.

*Graduate Student, Aeronautical/Astronautical Engineering Department.
†Professor, Aeronautical/Astronautical Engineering Department. Member AIAA.

Introduction

At present, spacecraft array sizes are limited by the severe weight restrictions of spaceflight. Using current construction techniques, these restrictions translate into maximum array sizes of around 10 m. Many space applications would be improved if the arrays could be enlarged. The larger size corresponds to greater focusing, collecting, or reflecting capabilities. In fact, some space applications such as optical communication links are not feasible until reflectors can be made on the order of 30–40 m in diameter. Therefore, new construction methods need to be explored.

One promising alternative construction technique involves the use of inflatable structural members. Recent NASA test flights using this type of construction have shown that arrays in the 30–40 m range are very attainable[1] and still well below the stringent weight requirements.[2] However, these same flight tests have revealed an inadequacy in deployment reliability. During inflation from the tightly packed launch configuration, the partially inflated membranes have a tendency to become entangled and to twist around each other, which leads to a deployment that is unpredictable and potentially catastrophic. Such behavior is also shown by simulation.[3] Deployment reliability is a major concern of the space community and must be addressed before inflatable structures can be used widely. This research is part of the effort to understand how the inflation process works. The final goal is eventually to control the inflation process and eliminate the deployment reliability problem.[4]

We have approached the problem by examining the inflation of a cylindrical Mylar tube. Specifically, we investigated how the forces and torques pertinent to deployment varied as functions of the internal pressure. To determine which forces and torques might be important, we had to consider how the membranes were packed prior to inflation. Membranes can be packed by either folding or rolling, as indicated in Fig. 1. These two possibilities have very different characteristics when inflated. Therefore two experiments were designed using the apparatus in Fig. 2: one to examine the forces at a fold and the other to characterize the torques on a rolled membrane.

The first experiment explores the forces caused by a fold in a membrane. When deflated, a folded membrane has fold lines that run flat and straight across the width. As air is introduced, the area behind the fold bulges and forms a pocket, but the fold line remains straight. Eventually, enough force is generated to open the fold so that air can leak into the next section of membrane. To simulate this process, a flat blade was pressed into the membrane until the membrane was

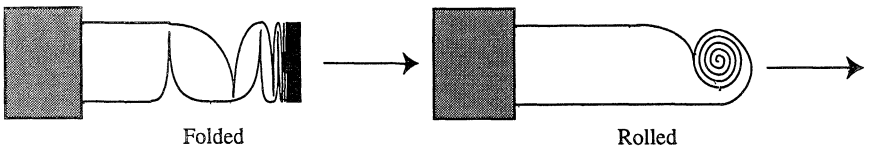

Fig. 1 Two common types of deployment.

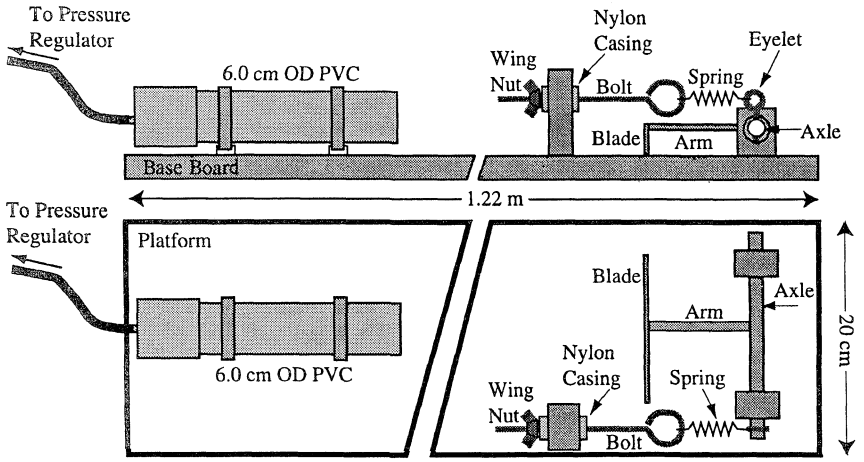

Fig. 2 Schematic of the experimental apparatus.

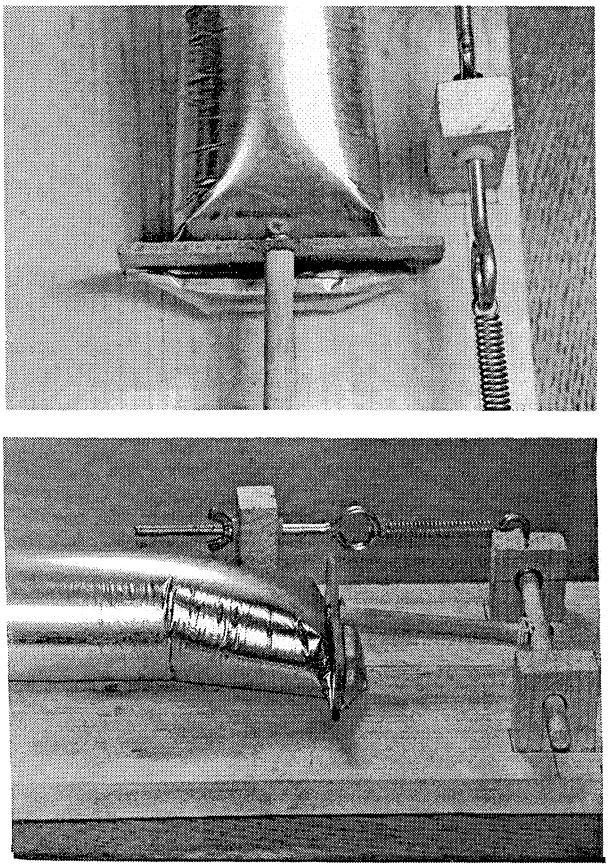

Fig. 3 Orthogonal views of the pinching-force experiment.

completely flat underneath the blade (Fig. 3). Like a fold line, the flat blade enforced the condition that the membrane be flat across its width. The force upward on the blade is equivalent to the force that would open a fold at that location. Thus the first experiment quantifies the relationship between the internal pressure and the force felt by the membrane at a fold line. Throughout this paper this experiment will be referred to as the pinching-force experiment.

The second experiment investigates the torques generated by inflating a rolled-up membrane. For this experiment the Mylar tube was wrapped around an axle. The torque on the axle could then be related to the internal pressure. This experiment will be referred to as the rolling-torque experiment.

Considerable work has been done on the analysis of inflated membranes. Particularly, the deployment of air bags and parachutes has received attention through the use of membrane finite elements.[5–7] In the general survey of nonlinear problems of shells,[8] the specific problems most relevant to deployment of complex structures are not included. Our hope was that a fundamental consideration may lead to a improvement in the situation. A relatively simple model was desired for two reasons. First, because the extensibility of the membrane can sometimes play a significant role, some finite element formulations would be forced to use full shell elements rather than inextensional membrane elements. Combine this with large deformations and contact regions and the problem becomes formidable. Second, we hoped that in the future dynamic experiments and calculations could be performed. Embedding a finite element model into the long time dynamic simulation of inflation would be even more costly.[4]

Experimental Apparatus

A device capable of inflating a cylindrical Mylar membrane, measuring the force upward on a flat blade and the torque exerted on an axle, was constructed. This device is shown in Fig. 2. The base consists of a 25 mm × 200 mm × 1.22 m platform. At one end a 60-mm-diam polyvinyl chloride (PVC) pipe runs along the center of the platform. The Mylar membrane fabricated for the experiment had a slightly larger diameter than the PVC pipe. The thickness of the membrane was 32 μm with a measured Young's modulus of 855 MPa. The membrane could be slipped over the end of the pipe and then fastened with a hose clamp. At the opposite end of the platform, a dowel and bearings formed an axle. A transverse hole at the midpoint of the axle allowed a blade/arm assembly to be attached. The blade/arm assembly was over 500 times more stiff than the spring. Thus the blade arm could be treated as a rigid member. For the pinching-force experiment the blade/arm assembly would be left in place. For the rolling-torque experiment the blade and arm would be removed, permitting the Mylar membrane to be wrapped directly around the axle. In either case we needed to be able to control and measure the torque on the axle.

Table 1 Calibration results

Calibration set	Slope (N/turn)	Intercept (N)	R^2
Without recalibration of the load cell each time	0.285	0.487	0.9995
	0.288	0.419	0.9998
	0.288	0.298	0.9998
With recalibration of the load cell each time	0.279	0.600	0.9995
	0.280	0.600	0.9987
	0.273	0.632	0.9994
	0.282	0.645	0.9995
Slope found using spring constant and kinematics	0.291	N/A	N/A
Mean value	0.283	0.526	
2σ	0.012	0.260	

To do this, an eyelet was screwed through the axle at one end. A spring connected the eyelet to a long bolt. The long bolt passed through a hole in the center of a hard nylon casing epoxied into a tall wooden block. A wing nut on the far end of the bolt pressed up against the nylon casing, preventing the bolt from being pulled back through the hole. The wing nut could be tightened, pulling the bolt farther through the hole. This adjusted the tension in the spring and ultimately the torque on the axle. Thus, the number of times the wing nut was turned could be used to determine the force on the blade or the torque exerted on the axle.

The next task was to calibrate the apparatus described in the preceding. Eight separate tests verified the linearity, the slope, and the intercept of the calibration curve. The results of the calibration tests are shown in Table 1.

For the calibration tests a load cell was connected directly to the flat blade attachment. The wing nut was tightened until the spring became perceptibly taught. This position became the zero turn position. After each full turn of the wing nut, a load cell reading was taken. In this way, the downward force on the blade could be related to the number of turns of the wing nut. After three consecutive tests the slopes were all consistent, but the intercept of each subsequent test was less than the previous one, which indicated some kind of slippage or drift in the system. In an attempt to track down the cause, a second set of calibrations were performed.

The only difference between the first set of calibrations and the second set was the recalibration of the load cell before each individual test. We feared that at low force levels the load cell would drift. The results of these tests had both a close grouping of slopes and a consistent value for the intercept.

Last, as a double check of our system, we directly measured the spring constant of the spring. Then using kinematics and the displacement associated with a turn of the wing nut, the force per wing nut turn could be independently calculated. This last value agreed with all of the other calibration results. To ensure an adequate measure of the uncertainty, we took the final calibration curve as the mean value of all of the tests, with an uncertainty equal to two standard deviations.

Pinching-Force Experiment

Experimental Procedure

A top and side view of the experiment in progress is shown in Fig. 3. The experiment began with the membrane completely deflated and the wing nut set to the zero turn position. Slowly, the pressure regulator was opened, and the membrane filled to a slightly positive gauge pressure. The wing nut was tightened until the blade returned to its initial position 1 mm above the base board. To help eliminate the effects of friction, we added lubricant at the contact line between the blade and the membrane. The number of wing nut turns and the internal pressure in the balloon were recorded. The internal pressure was then increased slightly. Again the wing nut was tightened until the force required to return the blade to the original position was achieved. This process was repeated until a maximum pressure of 3.0 kPa was reached. We then reversed the experimental process by decreasing the pressure and loosening the wing nut. In this way, we could check for any hysteresis in our experiment. No hysteresis was evident. Once the relationship between the internal pressure and the number of wing nut turns was known, the calibration curve could be used to find how the upward force on the blade varied with internal pressure. For the tests the axial prestress parameter

$$\rho = (PR^2/4Et^2)\sqrt{12(1-\nu^2)} \tag{1}$$

has the range (0.17, 2.59). Classical bifurcation buckling for axial stress occurs when this parameter equals -1 (Ref. 9). So the test pressure ranges from modest (0.2 kPa) to high (3 kPa) for this tube material and geometry.

Model for Pinch Experiment

Geometrical Observations

Experimental observations of the membrane geometry motivated the model. Figure 3 shows the actual geometry assumed by the membrane during experimentation. The main portion of the tube to the left of the blade retains the cylindrical shape, unaffected by the boundary condition enforced by the blade. As the membrane approaches the blade, it begins to flatten, eventually becoming completely flat as it passes underneath the blade. In particular, notice that the top portion of the membrane forms a curved sheet. This sheet appears to form a quarter of a cylinder running at 90 deg to the rest of the membrane. This cross-cylinder geometry allows the membrane to make a smooth transition from zero curvature in the long direction to zero curvature in the cross direction required by the flat-blade boundary condition. Also notice that this constraining sheet approaches both the blade and the main portion of the membrane in a tangent fashion.

Basic Membrane Principles

The basic principles involved are as follows[10]:

1) An inextensional surface of zero Gaussian curvature ($=1/R_1R_2$) must remain a surface of zero Gaussian curvature.

2) The Gaussian curvature can become positive or negative in a region of wrinkling. Wrinkling can only occur in one direction at a time.

3) For membrane equilibrium constant pressure loading will be carried by constant curvature.

4) A discontinuity in slope occurs only when an external line load or concentrated force is present. Therefore, when a membrane comes in contact with another surface without sticking, the membrane must be tangent to that surface at the contact point.

Using these principles as guides, we approximated the large deformation in Fig. 3 by local regions that are easily characterized. In Fig. 4 the cross cylinder on the top has the radius of curvature R_t while the small bubble on the right side of the blade has the radius of curvature R_b. The angle of the cross cylinder is θ_t. On the sides wrinkling occurs as seen in Fig. 3. However, any cross section of the cross cylinder or bubble in Fig. 4 must have the shape shown in Fig. 5. The points on the deformed cross section normal to the tube axis were originally on an elliptic section of the tube. The deformed shape is flat on the top, which is the region of curvature R_t in the orthogonal direction, and must be flat on the bottom, which is in contact with the rigid surface. The sides must be circular because they carry the pressure load. These principles in one form or another are often applied in the analysis of shells and membranes.[8] We show that they also can be used for the present complex configuration.

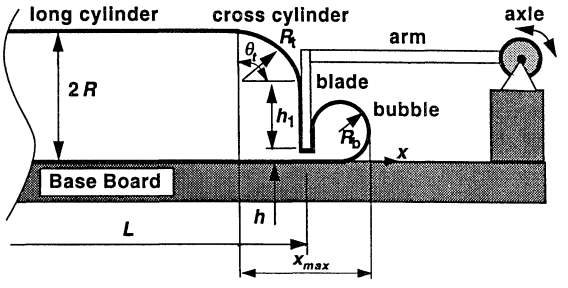

Fig. 4 Simplified geometry of pinching-force experiment. $L + L_3$ (not shown) is the total length of the membrane in a completely deflated state.

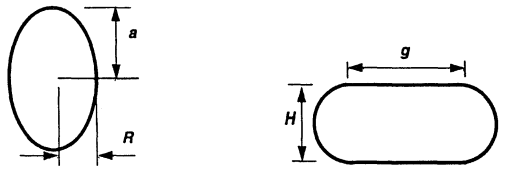

a) Initial elliptical cross section

b) Deformed shape

Fig. 5 Cross section of tube: a) before deformation, section at angle with axis, and b) after deformation, section normal to axis.

Mathematical Treatment

The idealized geometry is shown in Fig. 4. The initial flattened length of the tube is $L + L_3$:

$$L_3 = \tfrac{1}{2}\{R_b[1 + (3\pi/2)] + h_2 + h_1 + R_t(\theta_t - \sin\theta_t)\} \quad (2)$$

The radius at the top is

$$R_t = 2R - h_1 - h \quad (3)$$

and the contact height on the right side of the blade is

$$h_2 = R_b - h \quad (4)$$

However, according to principle 4, if the contact height on the left side h_1 is greater than zero, then the angle of contact θ_t must be $\pi/2$ by the contact tangency condition. If h_1 is zero, then the angle could be in the range, $0 < \theta_t \leq \pi/2$. Thus, these two parameters act as only one free parameter, so that in the total potential only h_1 is shown as an argument with the understanding that when h_1 is zero it is replaced by θ_t as the argument. The second free parameter is taken as the height of the blade from the lower surface h.

The total potential energy is

$$\Pi(h, h_1) = -P\,\mathrm{Vol}(h, h_1) + Fh + F\mu_{\mathrm{eff}} w(h, h_1) \quad (5)$$

where the length of material that slides underneath the end of the blade w is given by

$$w = R_t(\theta_t - \sin\theta_t) + h_1 \quad (6)$$

The effective friction coefficient is taken to be the friction for a cable wrapped around a curved surface[9]:

$$\mu_{\mathrm{eff}} = \frac{\exp\{\mu[(\pi/2) + \theta_t]\} - 1}{\exp\{\mu[(\pi/2) + \theta_t]\}\sin\theta_t + 1} \quad (7)$$

The approximation for the effect of friction should be reasonable for motion in one direction. The volume is

$$\mathrm{Vol} = \pi R^2(L - R_t \sin\theta_t) + \int_0^{x_{\max}} A\,dx \quad (8)$$

Figure 5 shows the idealized cross-section deformation used to calculate the volume change. For each cross section the top point experiences a shift in axial location with respect to the bottom point during deformation. This distance is given by Δx. This axial shift leads to the undeformed cross sections being ellipses rather than circles. The cross sections also undergo a contraction in the transverse direction given by Δz. Thus, with these reasonable geometric approximations the integrals for the potential energy equation (5) can be easily evaluated by numerical integration. Once we have chosen an h and h_1 (or θ_t), Δz and Δx are completely determined functions of x by using the simplified geometric assumptions. In the following equations we show explicitly the formulas necessary to compute the volume. The area of the deformed cross section is

$$A = \pi R^2[1 - (\Delta z/2R)][2s - 1 + (\Delta z/2R)] \quad (9)$$

in which the flattening of the section, shown in Fig. 5, is

$$H = 2R - \Delta z \quad (10)$$

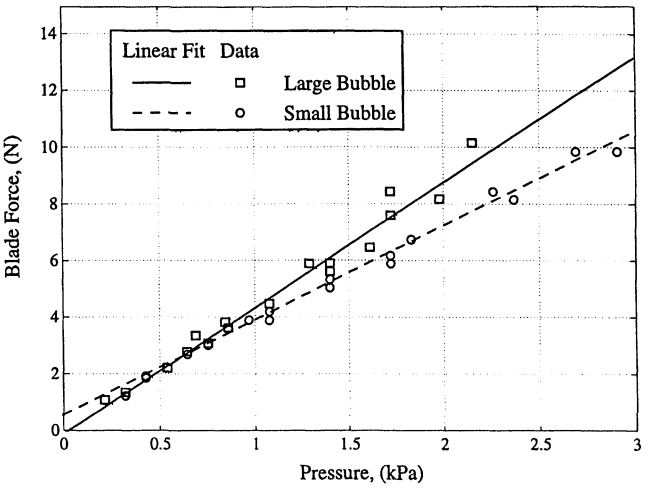

Fig. 6 Pinching-force experimental results with linear fit.

and s is the ratio of the perimeter of the ellipse to the perimeter of the cylinder. s can be found from the elliptic integral:

$$s = \left(\frac{a}{R}\right)^2 \frac{2}{\pi} \int_0^{\pi/2} \frac{1}{\{1 + [(\Delta x/2R)\sin\phi]^2\}^{\frac{3}{2}}}\,d\phi \quad (11)$$

The semimajor axis a is given by

$$a/R = [1 + (\Delta x/2R)^2]^{\frac{1}{2}} \quad (12)$$

Using these equations, the potential ends up as a function of only the two geometric parameters h and h_1 (or θ_t). By finding the minimum of this potential, we can obtain the equilibrium solution.

Pinching-Force Experimental and Modeling Results

Two sets of data are shown in Fig. 6. The difference between the two lies in the amount of material that extended beyond the blade. During the experiment, this extra material inflated to form a cross-cylinder bubble on the right side of the blade in Fig. 3. The more material beyond the blade, the larger the cylinder that forms. For the lower set of data, enough material extended beyond the blade to form a 6-mm-diam bubble, whereas for the upper set of data, there was enough material to form a 19-mm-diam bubble. Both sets of data show a linear relationship between the blade force and the internal pressure. The thin lines in Fig. 6 are best line fits of the data. So even for the moderate to lower values of pressure, the blade force is proportional to pressure, and the material properties of the tube wall are not significant. The reason for this is that the bubble radius R_b is kept as the reference, rather than the initial unloaded excess length. The approximation of inextensionality of the wall is correct for the deformation process. All of the measurements can be summarized into the statement

$$\frac{F}{P\pi R^2} = \begin{cases} 1.18 \pm 0.05 & \text{for } R_b/R = 0.1 \\ 1.57 \pm 0.067 & \text{for } R_b/R = 0.317 \end{cases} \quad (13)$$

Numerically, we found the minimum of the total potential given in Eq. (5). The results are shown in Fig. 7 for various values of the coefficient of friction μ. Figure 7 shows the dependence of the blade force on the radius of the small bubble at the tube end. The average of the experimental measurements at various levels of pressure are shown by the crossed squares. Apparently the coefficient of friction for the experiments was near 0.6 and 0.8 for the smaller and larger end radii, respectively. A friction value around 0.7 may be reasonable for Mylar on a wood edge with some lubrication. Only erratic measurements were obtained when the wood blade was dry.

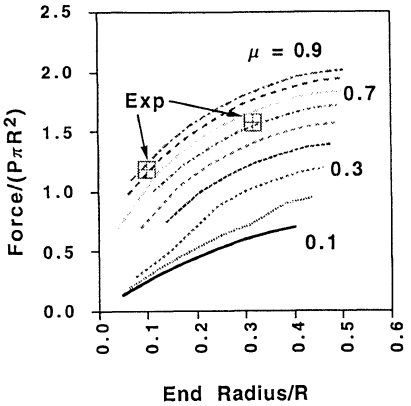

Fig. 7 Blade force for asymmetric pinch loading of finite length inflated tube. The family of curves shows the calculated effect of varying the friction coefficient μ. μ ranges from 0.1 to 0.9 in 0.1-sized increments.

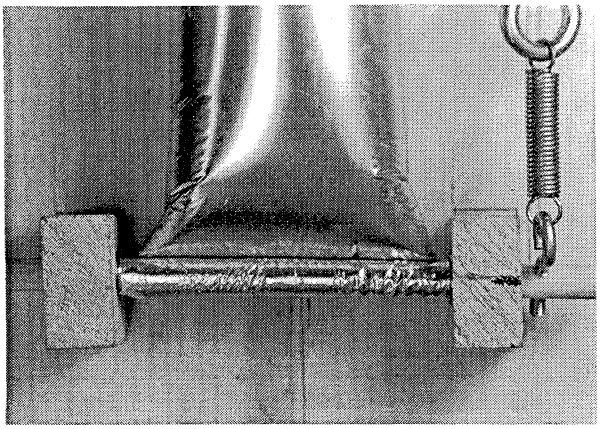

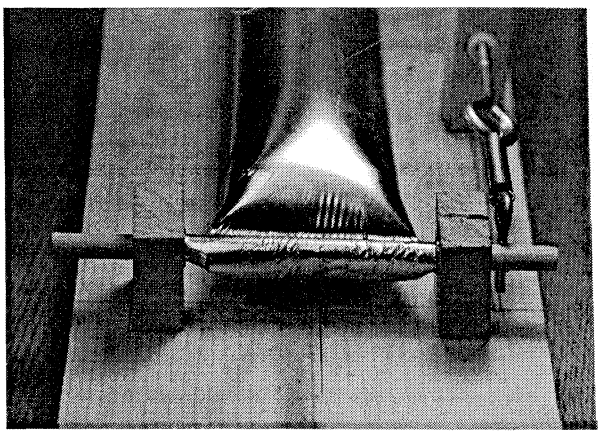

Fig. 8 Top and front views of the unrolling-torque experiment.

Unrolling-Torque Experiment

Experimental Procedure

Figure 8 shows the top and front views of the torque experiment in progress. This procedure was similar to the pinching-force experiment already described. After each increment in the pressure, the wing nut was turned until the axle returned to its original angular position. However, there were three differences between the two experiments. First, the blade and arm were removed from the apparatus, and the membrane was wrapped around the axle. Second, the previous calibration curve was modified to relate the axle torque to the number of turns. This was done by multiplying the existing curve by the distance between the blade and the center of the axle, 102 mm. Third, the maximum pressure was increased to 14.0 kPa [Eq. (1), $\rho = 12$] to get a sizable variation in the torque. All other aspects of the experimental procedure were the same.

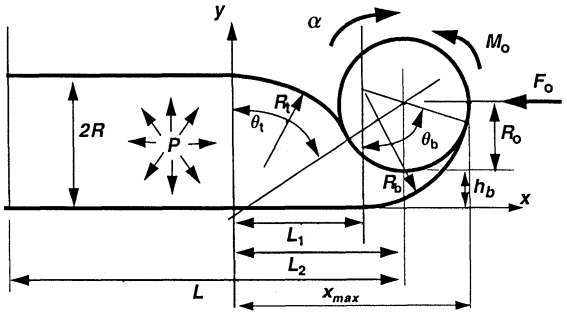

Fig. 9 Simplified geometry of torque experiment. $L + L_3$ (not shown) is the total length of the membrane in a completely deflated state.

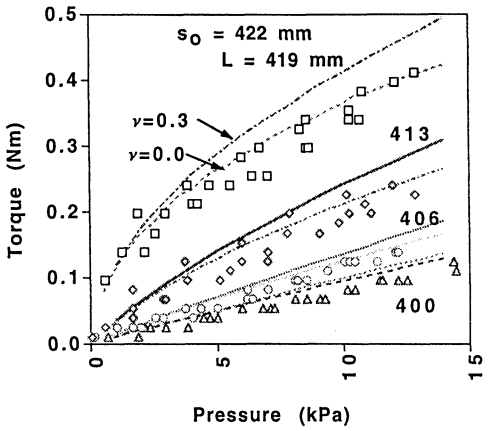

Fig. 10 Rolling torque: comparison of theory and experimental data. The initial deflated length of the membrane is s_0 = 422 mm. Experimental data are shown for four different values of the parameter L: □, L = 419 mm; ◇, L = 413 mm; ○, L = 406 mm; and △, L = 400 mm. The curves show the calculated response for ν = 0.0 and ν = 0.3 for each individual value of L.

Experimental Results

The geometry is shown in Fig. 9. The distance from the PVC pipe to the center of the axle is L. When the membrane is deflated, its length from the PVC pipe to the axle is $s_0 = L + L_3$. Thus L_3 is the initial excess length. Four sets of measurements are plotted in Fig. 10, each with a different length L while the initial deflated length s_0 is held fixed. When the difference is large, $s_0 \gg L$, the deflated membrane is loose. Consequently, with inflation the wrapping around the axle is substantial. On the other hand, when the difference is small, $L \to s_0$, the deflated membrane is taught between the PVC and the axle. Then with inflation, the wrapping is less. The corresponding increase in torque is clear in Fig. 10.

In the pinching-force experiment we lubricated the membrane under the blade. When the membrane was inflated, extra material could slide underneath the blade from the opposite side while the radius of the bubble was monitored. In the torque experiment the torque necessary to return the axle to the same position at each pressure was measured. Thus, the initial excess material remained constant throughout the experiment. A clear effect is that the torque in Fig. 10 is not linear with the pressure, particularly when the excess length is small. Thus the extension of the material can be significant.

Model for the Torque Experiment

Geometry

The actual geometry formed by the tube is shown in Fig. 8. The idealized side view is depicted in Fig. 9. The deflated portion of the tube is wrapped around the axle and forms a roll with the outer radius R_0. The roll has rotated through the angle α about the axle. On the left side at a distance from the axle greater than a diameter or so, the membrane retains the fully inflated cylindrical tube form with radius R. The geometry of the deformed region has common features with those in the pinching-force experiment. The top portion of the membrane forms the characteristic cross-cylinder geometry near the roll (principles 1, 3) with the radius R_t, subtending the angle

θ_t. The bottom portion of the membrane also forms a cross cylinder, but with a different radius R_b as it wraps around the roll through the angle θ_b. Note that the membranes must be tangent to the deflated material on the roll (principle 4). The length L is from the PVC tube to the axle of the roll. The axial distance between the centers of curvature of the top and bottom cross cylinders is L_1, which is also the axial length of the tube in contact with the lower rigid surface. The distance from the center of the top cross cylinder to the axle is L_2, and the height of the rigid surface to the roll around the axle is h_b. The condition that the arc length of the material unrolled from the top and bottom be equal is

$$(R_t + R_0)\theta_t = L_1 + (R_b - R_0)\theta_b \tag{14}$$

The other geometric relations are

$$L_2 = (R_t + R_0)\sin\theta_t = L_1 + (R_b - R_0)\sin\theta_b \tag{15}$$

$$(R_b - R_0)(1 - \cos\theta_b) = R + h_b - R_0 \tag{16}$$

$$(R_t + R_0)(1 - \cos\theta_t) = R - h_b + R_0 \tag{17}$$

With the elimination of L_1 and the radii R_b and R_t, the equations reduce to

$$\left(\frac{R - h_b + R_0}{R + h_b - R_0}\right)\frac{1 - \cos\theta_b}{\theta_b - \sin\theta_b} = \frac{1 - \cos\theta_t}{\theta_t - \sin\theta_t} \tag{18}$$

Therefore, with R, R_0, and h_b as input geometry, there is only one free geometric parameter. We take this to be the angle θ_b. For a given value of θ_b, the numerical solution of Eq. (18) yields θ_t, and consequently from Eqs. (15–17), the values of L_1, L_2, R_t, and R_b.

If there is no contact with the lower rigid surface, then $L_1 = 0$, the lower edge of the roll must be exactly on the long axis $h_b = R_0$, and the solution of Eq. (18) is $\theta_b = \theta_t$.

The volume is calculated with Eqs. (8–12) but now in the form

$$\text{Vol} = \text{Vol}(L, \theta_b) = \pi R^2(L - L_2) + \int_0^{x_{\max}} A\,dx \tag{19}$$

However, for handling the wrapping of the tube around the roll in the present case, using the arc length instead of the x coordinate as the integration variable is advantageous.

Potential Energy Formulation

The potential energy is similar to Eq. (5). However, because in this case, the initial excess length is monitored, the strain of the surface is significant. Even though the tube is essentially inextensional in the deformation process, a small strain multiplied by the length provides a significant additional excess length. The excess length of the deflated tube is the amount of material unrolled by rotating the axle through the angle α, less the distance from axle to end:

$$L_3 = \alpha R_0 - L = s_0 - L \tag{20}$$

For simplicity, the radius of the roll R_0 is taken as constant. The actual change in the roll radius with unrolling has no effect on these static results. After inflation, the excess length is increased by the average axial strain ε_1 and is related to the excess length in Fig. 9:

$$L_3 + L\varepsilon_1 = \alpha R_0 - L + L\varepsilon_1 = (R_b - R_0)(\theta_b - \sin\theta_b) \tag{21}$$

Thus the rotation angle can be considered as a function of the length, strain, and angle θ_b:

$$\alpha(L, \varepsilon_1, \theta_b) = (1/R_0)[L - L\varepsilon_1 + (R_b - R_0)(\theta_b - \sin\theta_b)] \tag{22}$$

The total potential is written as

$$\Pi(L, \varepsilon_1, \varepsilon_2, \theta_b) = -P\,\text{Vol}(L, \theta_b) + FL + T\alpha + \left[\frac{Et}{2(1 - \nu^2)}\left(\varepsilon_1^2 + 2\nu\varepsilon_1\varepsilon_2 + \varepsilon_2^2\right) - PR\varepsilon_2\right]2\pi RL \tag{23}$$

in which the torque on the axle is T and the force on the axle is F, as shown in Fig. 9.

The variation of Eq. (23) with respect to the circumferential strain ε_2 just yields the circumferential stress resultant in the main portion of the tube N_2:

$$N_2 = [Et/(1 - \nu^2)](\varepsilon_2 + \nu\varepsilon_1) = PR \tag{24}$$

and the variation with respect to the axial strain ε_1 yields the average axial resultant N_1:

$$N_1 = \frac{Et}{1 - \nu^2}(\varepsilon_1 + \nu\varepsilon_2) = \frac{T}{R_0 2\pi R} \tag{25}$$

which gives the average axial strain:

$$\varepsilon_1 = \frac{PR}{2Et}\left(\frac{T}{P\pi R^2 R_0} - 2\nu\right) \tag{26}$$

The variation of the potential Eq. (23) with respect to the length L, after dropping the small strain terms, yields

$$FR_0 + T = P\pi R^2 R_0 \tag{27}$$

which is a surprising result. The total torque, which is acting about the lower point of the roll and is the torque causing unrolling, is simply the pressure times area of the tube times the radius of the roll. Finally, the torque about the axle is obtained by taking the variation of Eq. (22) with respect to θ_b:

$$-P\frac{\partial}{\partial\theta_b}\text{Vol} + T\frac{\partial\alpha}{\partial\theta_b} = 0 \tag{28}$$

An efficient computation procedure is the reverse method. For a given θ_b Eq. (28) gives the torque T, then Eq. (27) the force F, then Eq. (26) the strain ε_1, and finally Eq. (21) the original excess length L_3.

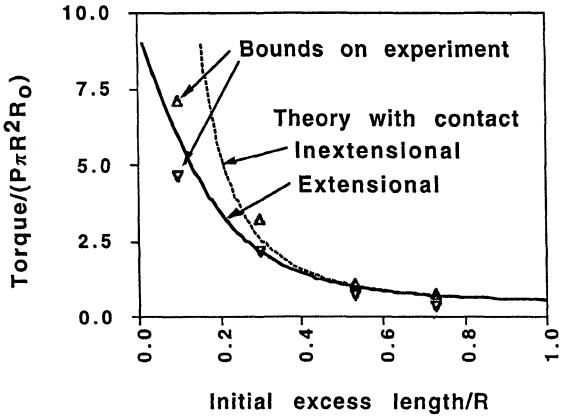

Fig. 11 Comparison of experimental results and calculations for the torque on the roll axial for low pressure P = 2 kPa.

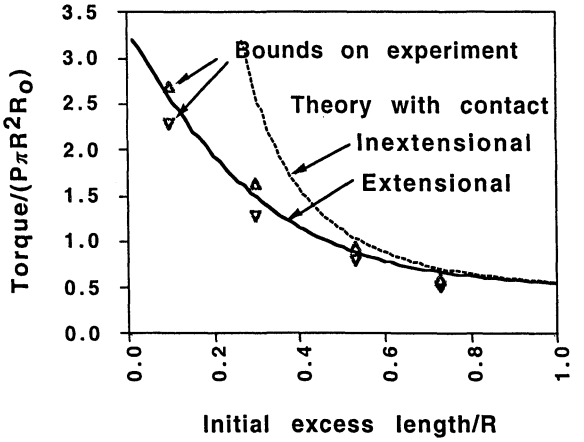

Fig. 12 Comparison of experimental results and calculations for the torque on the roll axial for high pressure P = 10 kPa.

Comparison of Experimental and Modeling Results

The theoretical results from Eq. (23) are shown by the solid and dashed curves in Fig. 10. The calculations for Poisson's ratio of $\nu = 0$ are close to the mean of the experimental points. However, the value of $\nu = 0.3$ is probably more reasonable for the Mylar. Thus the theoretical values are slightly high, indicating that the theoretical model is stiffer than the reality of the experimental configuration. In Fig. 11 the results are shown for the dimensionless torque as a continuous function of the excess length for the fixed pressure of 2 kPa. The theoretical curves are for $\nu = 0$. Bounds on the experimental values from Fig. 10 are included. Also shown is the result for inextensional material, which gives much higher torque values for small excess length. This is more so the situation for the larger pressure of 10 kPa shown in Fig. 12.

Conclusions

The deployment of large inflatable structures is a complex problem and a substantial challenge for simulation. No matter how complex, however, either the z fold or the roll in Fig. 1, or a combination, will be key features. We have addressed each with a simple measurement. The results provide bench mark problems for any computational procedure. However, we have proposed a theoretical formulation that provides an efficient method for the computation of the significant forces. In the formulation the difficult features of large deformation, high prestress, near inextensionality, and unknown regions of contact are easily handled. Although improvements in the formulation can be made, the results obtained are in sufficiently good agreement with the experiments that we anticipate the theoretical approach to be valid in many other configurations. In simulation of the dynamic deployment, often a good approximation is that the inertia is in the straight links and/or roll and that the joint forces and torques are quasistatic.[3,6] For such simulations the present theory should be directly useful.

References

[1]Cassapakis, C., and Thomas, M., "Inflatable Structures Technology Overview," AIAA Paper 95-3738, Oct. 1995.

[2]Casper, J. H., Brown, C. L., Thomas, A. S. W., Bursch, D. W., Runco, M., and Garneau, M., "Preliminary Mission Report: Spartan 207/Inflatable Antenna Experiment Flown on STS-77," NASA Goddard Space Flight Center, Greenbelt, MD, Feb. 1997.

[3]Tsoi, S. H. H., "Modeling and Simulation of Inflatable Space Structures," Engineer's Thesis, Dept. of Aeronautics and Astronautics, Stanford Univ., Stanford, CA, June 1997.

[4]Haug, E., Protard, J. B., and Milcent, G., "The Numerical Simulation of the Inflation Process of Space Rigidized Antenna Structures," *Proceedings of the International Conference on Spacecraft Structures and Mechanical Testing*, Vol. 2, edited by W. R. Burke, ESA, Paris, 1991, pp. 861–869.

[5]Hoffman, R., Pickett, A. K., Ulrich, D., Haug, E., Lasry, D., and Clinkemaillie, J., "A Finite Element Approach to Occupant Simulation: The PAM-CRASH Airbag Model," Society of Automative Engineers, SAE Paper 890754, 1989.

[6]Jenkins, C. H., "Nonlinear Dynamic Response of Membranes: State of the Art-Update," *Applied Mechanics Reviews*, Vol. 44, No. 7, 1991, S41-48.

[7]Lakshminarayan, V., and Lasry, D., "Finite Element Simulation of Driver Folded Air Bag Deployment," Society of Automative Engineers, SAE Paper 912904, 1991.

[8]Libai, A., and Simmonds, J. G., *The Nonlinear Theory of Elastic Shells*, Cambridge Univ. Press, New York, 1998.

[9]Lorenz, R., "Achsensymmetrische Verzerrungen in Dunnwandigen Hohozylindern," *Zeitschrift des Vereines Detscher Ingenieure*, Vol. 52, No. 43, 1908, pp. 1706–1713 (Sec. 7.5).

[10]Love, A. E. H., *The Mathematical Theory of Elasticity*, 4th ed., Dover, New York, 1944, Chaps. 23, 24.

R. B. Malla
Associate Editor